HHS Public Access

Author manuscript

Magn Reson Med. Author manuscript; available in PMC 2023 February 01.

Published in final edited form as:

Magn Reson Med. 2023 February ; 89(2): 636–651. doi:10.1002/mrm.29475.

NOE-weighted imaging in tumors using low-duty-cycle 2π-CEST

Jing Cui[1,2], **Casey Sun**[1,3], **Zhongliang Zu**[1,2]

[1]Vanderbilt University Institute of Imaging Science, Nashville, US

[2]Department of Radiology and Radiological Sciences, Vanderbilt University Medical Center, Nashville, US.

[3]Department of Chemistry, University of Florida, Gainesville, US.

Abstract

Purpose: Nuclear Overhauser enhancement (NOE)-mediated chemical exchange saturation transfer (CEST) imaging at −3.5ppm has shown clinical interest in diagnosing tumors. Multiple-pool Lorentzian fit has been used to quantify NOE, which, however, requires a long scan time. Asymmetric analysis of CEST signals could be a simple and fast method to quantify this NOE. But it has contamination from the amide proton transfer (APT) at 3.5ppm. This work proposes a new method using an asymmetric analysis of a low-duty-cycle pulsed-CEST sequence with a flip angle of 360°, termed 2π-CEST, to reduce the contribution from APT.

Methods: Simulations were used to evaluate the capability of the 2π-CEST to reduce APT. Experiments on animal tumor models were performed to show its advantages compared with the conventional asymmetric analysis. Samples of reconstituted phospholipids and proteins were used to evaluate the molecular origin of this NOE.

Results: The 2π-CEST has reduced contribution from APT. In tumors where we show that the NOE is comparable to the APT effect, reducing the contamination from APT is crucial. The results show that the NOE signal obtained with 2π-CEST in tumor regions appears more homogeneous than that obtained with the conventional method. The phantom study showed that both phospholipids and proteins contribute to the NOE at −3.5ppm.

Conclusion: The NOE at −3.5ppm has a different contrast mechanism from APT and other CEST/NOE effects. The proposed 2π-CEST is more accurate than the conventional asymmetric analysis in detecting NOE, and requires much less scan time than the multiple-pool Lorentzian fit.

Keywords

Chemical exchange saturation transfer (CEST); nuclear Overhauser enhancement (NOE); magnetization transfer (MT); tumor

Correspondence to: Zhongliang Zu, Ph.D., Vanderbilt University Institute of Imaging Science, 1161 21st Ave. S, Medical Center North, AAA-3112, Nashville, TN 37232-2310, zhongliang.zu@vumc.edu, Phone: 615-875-9815, Fax: 615-322-0734.

INTRODUCTION

Chemical exchange saturation transfer (CEST) is an emerging MRI contrast mechanism that is based on the saturation transfer between exchangeable or coupling solute protons and water protons (1–5). Nuclear Overhauser enhancement (NOE)-mediated saturation transfer is a type of CEST effect that is based on the dipolar interaction between motionally restricted protons and water protons (6–8). In CEST/NOE imaging, exchanging/coupling protons are selectively saturated by a radiofrequency (RF) saturation block, which then exchange or interact with water protons. After a long (e.g., a few seconds) saturation, an accumulative exchanging/coupling effect causes a substantial change in the water signal. By measuring the water signal, CEST/NOE provides an amplification process to detect solute molecules with low concentration and/or extremely short transverse relaxation time (T_{2s}) that otherwise cannot be directly observed (9).

In CEST/NOE imaging, a Z-spectrum, which is a plot of the water signal as a function of RF frequency offset, is usually obtained so that each CEST/NOE effect can be identified. In biological tissues, these CEST/NOE effects are usually in a frequency range between −5ppm to 5ppm, including the amide proton transfer (APT) effect at 3.5ppm (10,11), amine-water saturation transfer effects between 2ppm and 3ppm (12–15), the NOE effect at −1.6ppm (16–22), and the NOE effect at −3.5ppm (23,24). These CEST/NOE effects arise from the exchanging/coupling protons of different molecules that have different exchanging/coupling rates (k_{sw}) and/or T_{2s}: the APT effect has been assigned to be from the amide protons on the backbone of mobile proteins/peptides which are in the slow exchange regime (dozens of s^{-1}) (11,25); the amine-water saturation effects have been assigned to be from the amine protons of creatine (14,15,26–29), glutamate (12,30–32), and proteins (33,34) which are in the intermediate to fast exchange regime (a few hundred to a few thousand s^{-1}); the NOE at −1.6ppm has been assigned to be from the choline head group of phospholipids which is in the slow coupling regime; the NOE at −3.5ppm has been assigned to be from mobile macromolecular components with finite linewidth which is also in the slow coupling regime (35,36). In addition to these CEST/NOE effects, direct water saturation (DS) and magnetization transfer (MT) effects can also be observed on the CEST Z-spectra, which overlap with these CEST/NOE effects and always cause difficulty in the accurate and specific quantification of these effects. The MT effect is attributed to rigid macromolecules (e.g. myelin), which have a very broad peak beyond ± 5ppm. The peak of the NOE effect at −3.5ppm is usually broader than other CEST/NOE effects but much narrower than the MT effect. This suggests that the T_{2s} of the exchanging/coupling protons that contribute to the NOE effect at −3.5ppm should be shorter than those that contribute to other CEST/NOE effects but longer than those that contribute to the MT effect.

At relatively low saturation powers, the amplitude of the NOE effect at −3.5ppm is usually larger than that of other CEST/NOE effects. It can be clearly observed in nearly all biological tissues, including the brain (23,24), muscle (37), kidney (38), and spinal cord (39). Previously, the NOE effect at −3.5ppm has shown clinical interest in diagnosing tumors (23,40–45). Isolating the NOE effect at −3.5ppm from nonspecific DS, MT, and/or other CEST/NOE effects is crucial for accurate and specific quantification. Additionally, fast data acquisition and processing are important for clinical and preclinical applications.

The NOE effect at −3.5ppm has been quantified by Lorentzian difference (LD) analysis (23), multiple-pool Lorentzian fit (17), the three-point method (46), and asymmetric analysis of the magnetization transfer ratio (MTR_{asym}) (41). However, both the LD analysis and multiple-pool Lorentzian fit require the acquisition of the whole Z-spectrum for the fitting of reference signals or each CEST/NOE peak, which takes a long imaging time and relies on the initial values of the fitting parameters; the three-point method uses the average of two nearby signals (e.g., −2ppm and −5ppm) as a reference to remove the DS and MT effects, which is faster than the LD analysis and the multiple-pool Lorentzian fit methods but may underestimate the NOE effect (47); the asymmetric analysis method uses the CEST signal at the offset frequency symmetric about the water resonance as a reference to remove the DS and MT effects (assuming MT is symmetric about water). This asymmetric analysis method is also faster than other methods, and the data processing is simple. However, there is contamination from the APT effect at 3.5ppm in the quantification of the NOE effect at −3.5ppm.

The CEST saturation block could be either a continuous wave RF saturation pulse (CW-CEST) or a series of shaped RF saturation pulses with interleaved spoiler gradients (pulsed-CEST). In CW-CEST imaging, the saturation power (ω_1) is usually adjusted to optimize the CEST signal by balancing the saturation efficiency, DS effect, and MT effect. In pulsed CEST imaging, an average saturation power (average ω_1) can be obtained by adjusting the saturation pulse flip angle (θ), saturation pulse duration (τ_s), and exchange duration between two adjacent saturation pulses (τ_{ex}), which can be used to optimize the CEST signal. Compared with the CW-CEST, the pulsed-CEST provides additional dials to control the spin labeling and transfer effects. For example, when τ_s is comparable to T_{2s} and $1/k_{sw}$, the solute spins are rotated to a flip angle close to θ after a single saturation pulse; when the duty cycle is also low (i.e., $\tau_{ex} > \tau_s$), the solute spins recover to a dynamic equilibrium after an exchange duration so that they can be rotated to θ again during the next saturation pulse, allowing an accumulative rotation transfer effect. Different from the conventional saturation transfer effect with which the spins have nearly no or very small rotation, this rotation transfer effect is more sensitive to the solute relaxation and exchange properties, which allows the separation of different CEST/NOE effects. Previously, we developed a method using the subtraction of two pulsed-CEST sequences with two different θ (i.e., π and 2π) but the same average ω_1, termed chemical exchange rotation transfer (CERT) (48–54), to isolate the CEST effect of slow exchanging pools from the CEST effect of the fast exchanging pools, DS and MT effects. This method can isolate APT, guanidino amine CEST, and the NOE effect at −1.6ppm, but not the NOE effect at −3.5ppm, from confounding factors. In this paper, we developed a new method by using a low-duty-cycle pulsed-CEST sequence with a θ of 360° together with asymmetric analysis, termed 2π-CEST, to isolate the NOE effect at −3.5ppm from confounding factors and applied it to quantify variations in the NOE effect at −3.5ppm in tumors.

METHODS

2π-CEST sequence and quantification metrics

The 2π-CEST saturation block contains a series of low-duty-cycle trains of 2π pulses, which is designed to minimize the relative contribution from the APT effect to the NOE effect at −3.5ppm, through which we can use asymmetric analysis to remove the DS and MT effects and isolate a more accurate NOE effect. Here, we term the asymmetric analysis of CW-CEST signals (S_{CW}) as MTR_{asym_CW} and the asymmetric analysis of 2π-CEST signals ($S_{2\pi}$) as $MTR_{asym\_2\pi}$,

$$MTR_{asym\_CW}(\Delta\omega) = \frac{S_{CW}(-\Delta\omega)}{S_0} - \frac{S_{CW}(+\Delta\omega)}{S_0} \quad (1)$$

$$MTR_{asym\_2\pi}(\Delta\omega) = \frac{S_{2\pi}(-\Delta\omega)}{S_0} - \frac{S_{2\pi}(+\Delta\omega)}{S_0} \quad (2)$$

where (+) represents the resonance frequency offset of the labeled protons, (−) is the offset on the opposite side of the water peak, Δω is the RF saturation pulse frequency offset from water, S is the measured signal with RF saturation, and S_0 is the control signal acquired without RF saturation.

This direct subtraction of S(+Δω) and S(-Δω) cannot fully remove the DS and MT effects due to the shine-through effect and also has influence from the apparent water longitudinal relaxation rate (R_{1obs} =1/T_{1obs}) (55,56). Therefore, an inverse subtraction analysis with correction of R_{1obs} termed apparent exchange-dependent relaxation (AREX), has been used to improve the specificity in quantifying CEST/NOE effects (56). Here, we also combine AREX with the asymmetric analysis of the CW-CEST signals and the 2π-CEST signals, termed $AREX_{asym\_CW}$ and $AREX_{asym\_2\pi}$, respectively,

$$AREX_{asym\_CW}(\Delta\omega) = \left(\frac{S_0}{S_{CW}(+\Delta\omega)} - \frac{S_0}{S_{CW}(-\Delta\omega)}\right)R_{1obs}(1 + f_m) \quad (3)$$

$$AREX_{asym\_2\pi}(\Delta\omega) = \left(\frac{S_0}{S_{2\pi}(+\Delta\omega)} - \frac{S_0}{S_{2\pi}(-\Delta\omega)}\right)R_{1obs}(1 + f_m) \quad (4)$$

where f_m is the MT pool concentration. Here, the term (1+ f_m) was added to Eq. (3) and Eq. (4) to further improve their specificity to the solute protons when the MT pool is present (56).

Multiple-pool Lorentzian fit

Multiple-pool Lorentzian fit of CW-CEST Z-spectrum was performed to quantify each CEST/NOE pool. Eq. (5) provides the model function of the Lorentzian fit method.

$$\frac{S(\Delta\omega)}{S_0} = 1 - \sum_{i=1}^{N} L_i(\Delta\omega) \quad (5)$$

Here, $L_i(\Delta\omega)=A_i/(1+(\Delta\omega-\Delta_i)^2/(0.5W_i)^2)$, which represents a Lorentzian line with central frequency offset from water (Δ_i), peak full width at half maximum (W_i), and peak amplitude (A_i). N is the number of fitted pools. A six-pool model Lorentzian fit including amide (L_1), amine (L_2), water (L_3), NOE(−1.6) (L_4), NOE(−3.5) (L_5), and MT (L_6) was performed to process the Z-spectra. The fitting was performed to achieve the lowest RMS of residuals between the measured data and model. Supporting Information Table S1 lists the starting points and boundaries of the fit. The label signal (S_{lab}) was obtained by the summation of all Lorentzians. The reference signal (S_{ref}) for quantifying a CEST, NOE, or MT effect was obtained by the summation of all Lorentzians except the corresponding pool. The multiple-pool Lorentzian fitted CEST/NOE effects from the CW-CEST signals are quantified by $MTR_{multifit\_CW}$ and $AREX_{multifit\_CW}$,

$$MTR_{multifit\_CW}(\Delta\omega) = \frac{S_{ref}}{S_0} - \frac{S_{lab}}{S_0} \quad (6)$$

$$AREX_{multifit\_CW}(\Delta\omega) = \left(\frac{S_0}{S_{lab}} - \frac{S_0}{S_{ref}}\right) R_{1obs}(1 + f_m) \quad (7)$$

$MTR_{multifit\_CW}$ for MT effect was also obtained by Eq. (6). $AREX_{multifit\_CW}$ for MT was obtained by $R_{1obs}L_6/(1-L_6)$ (Supplementary Information Theory). Asymmetric analysis of each multiple-pool Lorentzian fitted CEST/NOE/MT spectrum, termed $MTR_{asym\_multifit\_CW}$ or $AREX_{asym\_multifit\_CW}$, were then obtained using Eq. (1) and Eq. (3) by replacing S_{cw} with $MTR_{multifit\_CW}$ or $AREX_{multifit\_CW}$ for each pool. Since MTR_{asym_CW} and $AREX_{asym\_CW}$ are roughly equal to the sum of $MTR_{asym\_multifit\_CW}$ and $AREX_{asym\_multifit\_CW}$ from all pools, $MTR_{asym\_multifit\_CW}$ and $AREX_{asym\_multifit\_CW}$ were used to evaluate the contribution from each pool to MTR_{asym_CW} and $AREX_{asym\_CW}$. $MTR_{asym\_multifit\_CW}$ and $AREX_{asym\_multifit\_CW}$ for the MT pool represent the contribution from MT asymmetry (57).

Simulations

The 2π-CEST signals were simulated with a three-pool (solute, water, and MT) model simulation of coupled Bloch equations. The CW-CEST signals were also simulated with ω_1 the same as the average ω_1 of the 2π-CEST for comparison. $AREX_{asym\_cw}$, $AREX_{asym\_2\pi}$, MTR_{asym_cw}, and $MTR_{asym\_2\pi}$ were calculated based on Eqs. (1–4). The ratio of $AREX_{asym\_2\pi}$ to $AREX_{asym\_cw}$ and the ratio of $MTR_{asym\_2\pi}$ to MTR_{asym_cw} were used to evaluate the signal selectivity of the 2π-CEST sequence for measuring APT and NOE effects compared with the CW-CEST sequence. The ratio of $AREX_{asym\_2\pi}$ or $AREX_{asym\_cw}$ for measuring APT to that for measuring NOE was also used to evaluate the relative contribution from the APT effect to the NOE effects. In simulation #1, we utilized varied sequence parameters but two sets of constant sample parameters mimicking both amide and macromolecular protons: the 2π-CEST sequence parameters were varied with

duty cycle from 20% to 80% for a few τ_s (5s to 30s); the amide and macromolecular protons have a solute concentration of (0.005, 0.005), k_{sw} of ($50s^{-1}$, $50s^{-1}$), solute longitudinal relaxation times (T_{1s}) of (1.5s, 1.5s), T_{2s} of (20ms, 0.5ms), and solute resonance frequency offsets of (+3.5ppm, −3.5ppm) corresponding to (1400Hz, −1400Hz at 9.4T). In simulation #2, we used varied sample parameters but constant sequence parameters: τ_s and the duty cycle of the 2π-CEST sequence are 13ms and 18.1%, respectively, corresponding to an average ω_1 of 1μT; k_{sw} was varied from $20s^{-1}$ to $5000s^{-1}$ with other sample parameters kept constant and the same as those in simulation #1; T_{2s} was varied from 0.5ms to 50ms with other sample parameters kept constant and the same as those in simulation #1. In simulation #3, a certain set of sequence and sample parameters but varied B_1 shift (from 80% to 120% of the nominal values with a step of 0.5%) and B_0 shift (−20 to 20 Hz with a step of 0.5 Hz) was employed: the B_1 shift in the 2π-CEST imaging causes changes in the saturation pulse flip angle and average ω_1, but not changes in τ_s and duty cycle which are kept at 13ms and 18.1%, respectively; the sample parameters are the same as those for the macromolecular protons in simulation #1. The sample parameters from water (w) and MT (m) pools include the concentration (f_w, f_m) of (1, 0.1), (T_{1w}, T_{1m}) of (1.5 s, 1.5 s), (T_{2w}, T_{2m}) of (50ms, 15μs), k_{sw} of ($0s^{-1}$, $25s^{-1}$), and the resonance frequency offsets of (0ppm, 0ppm). R_{1obs} was obtained by using Eq. (8) according to Ref (56),

$$R_{1obs} \approx (1/T_{1w} + f_m/T_{1m})/(1 + f_m) \tag{8}$$

The coupled Bloch equations can be written as $\frac{d\mathbf{M}}{dt} = \mathbf{AM} + \mathbf{M_0}$, where A is a 7 × 7 matrix for the three-pool model. The water and solute pools each have three coupled equations representing their x, y, and z components. The MT pool has a single coupled equation representing the z component, with a Lorentzian absorption line shape (58). The total saturation time for the CW-CEST and the 2π-CEST is 5s. All numerical calculations of the CEST/NOE signals integrated the differential equations through the sequence using the ordinary differential equation solver (ODE45) in MATLAB 2018a (Math works, Natick, MA, USA).

Phantom preparation

Samples of reconstituted phospholipids from egg phosphatidylcholine (Egg PC), bovine serum albumin (BSA), and egg white albumen (EWA) were used to evaluate the molecular origin of the NOE effect at −3.5ppm. The Egg PC sample was prepared by first dissolving it together with cholesterol in chloroform. The chloroform was then removed under an air stream and vacuum. The lipids were resuspended in water at a ratio of 1:3 (lipid to water) by weight. The suspension was sonicated in a bath sonicator, and was frozen and thawed for a few cycles to produce liposomes. The BSA and EWA samples were prepared by adding 10% (weight/weight) BSA or EWA to phosphate buffered saline (PBS) at pH 7.

Animal Preparation

Three rats bearing 9L tumors were included in this study. For brain tumor induction, each rat was injected with 1×10^5 9L glioblastoma cells in the right brain hemisphere, and was then imaged after 2 to 3 weeks. All rats were immobilized and anesthetized with

a 2%/98% isoflurane/oxygen mixture during data acquisition. Respiration was monitored to be stable, and a constant rectal temperature of 37 °C was maintained throughout the experiments using a warm-air feedback system (SA Instruments, Stony Brook, NY, USA). All animal procedures were approved by the Animal Care and Usage Committee of Vanderbilt University Medical Center.

MRI

In the 2π-CEST sequence, $\theta = 360°$, $\tau_s = 13$ms, and $\tau_{ex} = 59.2$ms, corresponding to an average ω_1 of 1μT and duty cycle of 18.1%. The pulses were repeated 69 times or 110 times so that the total saturation time (T_{sat}) was 5s (animals) or 8s (phantoms), respectively. The 2π-CEST blocks are followed by a single-shot spin-echo echo planar imaging (SE-EPI) readout (animals) or a free induction decay (FID) acquisition (phantoms) and a recovery time of 2s before the next experiments. The CW-CEST contains a 5s rectangular RF pulse with ω_1 of 1μT, followed by a single-shot SE-EPI readout and a recovery time of 2s. TE for the SE-EPI readout is 13ms and TR is 7s. . The 2π-CEST Z-spectra were acquired with RF offsets from −2000 to 2000 Hz with a step of 50 Hz (−5 to 5 ppm on 9.4 T). The CW-CEST Z-spectra were acquired with RF offsets at ±4000, ±3500, ±3000, ±2500, and from −2000 to 2000 Hz with a step of 50 Hz (−10 to 10 ppm on 9.4 T). The Control signal was obtained by setting the RF offset to 100000 Hz (250ppm on 9.4 T). R_{1obs} and f_m were obtained using a selective inversion recovery (SIR) method with inversion times of 4, 5, 6, 8, 10, 12, 15, 20, 50, 200, 500, 800, 1000, 2000, 4000, and 6000ms (59). All images were acquired with matrix size 64 × 64, field of view 30mm × 30mm, slice thickness of 2mm, and one average. Experiments were performed on a Varian DirectDrive™ horizontal 9.4T magnet with a 38-mm Litz RF coil (Doty Scientific Inc. Columbia, SC).

Data analysis and statistics

Regions of interest (ROIs) of tumors were outlined from the f_m map with values less than a threshold of 7%. ROIs of contralateral normal tissue were chosen to mirror the tumor ROIs. Student's t-test was employed to evaluate the signal difference. Differences were considered to be statistically significant when $P < 0.05$. All data analysis and statistical analyses were performed using MATLAB 2018a (Math works, Natick, MA, USA).

RESULTS

Fig. 1a, 1b, 1e, and 1f show the ratio of $AREX_{asym\_2\pi}$ to $AREX_{asym\_cw}$ and the ratio of $MTR_{asym\_2\pi}$ to MTR_{asym_cw} vs. duty cycle from the simulated CW-CEST and 2π-CEST signals with varied sequence parameters but constant sample parameters. Compared with the $AREX_{asym\_CW}$ and the MTR_{asym_CW} values, the $AREX_{asym\_2\pi}$ and the $MTR_{asym\_2\pi}$ values for amide protons with lower duty cycles have greater reductions than those for macromolecular protons. For the duty cycle of 20% and τ_s of 10ms as an example, although $AREX_{asym\_2\pi}$ is 70.4% of the corresponding $AREX_{asym\_CW}$ for macromolecular protons, $AREX_{asym\_2\pi}$ is 22.5% of the corresponding $AREX_{asym\_CW}$ for amide protons. This suggests that the low-duty-cycle 2π-CEST has more signal selectivity than the high-duty-cycle 2π-CEST and the CW-CEST. Additionally, note that this signal selectivity is relatively insensitive to τ_s in the parameter range in this simulation. Fig. 1c, 1d, 1g, and

1h show the scatter plots of all the $AREX_{asym\_CW}$, $AREX_{asym\_2\pi}$, MTR_{asym_CW}, and $MTR_{asym\_2\pi}$ values from Fig. 1a, 1b, 1e, and 1f as a function of ω_1 or average ω_1. Note that although the $AREX_{asym\_CW}$ values for amide protons as well as the $AREX_{asym\_CW}$ and the $AREX_{asym\_2\pi}$ values for macromolecular protons simply increase with ω_1 or average ω_1, the $AREX_{asym\_2\pi}$ values for amide protons do not have a simple relationship with average ω_1. This suggests that the CW-CEST imaging of both the APT effect and the NOE effect at −3.5ppm as well as the 2π-CEST imaging of the NOE effect at −3.5 ppm have a saturation transfer effect that mainly depends on ω_1 or average ω_1. In contrast, the 2π-CEST imaging of the APT effect has the rotation transfer effect, which depends on not only average ω_1 but also other sequence parameters. Supporting information Table S2 lists the ω_1 and the corresponding τ_s, τ_{ex}, duty cycle, number of pulses, and T_{sat} in the 2π-CEST imaging in Fig. 1c, 1d, 1g, and 1h. Supporting information Figure S1 shows the scatter plots of the corresponding τ_s, τ_{ex}, and duty cycle in the 2π-CEST imaging in Fig. 1c, 1d, 1g, and 1h as a function of average ω_1. Note that the pattern of $AREX_{asym\_2\pi}$ values vs. average ω_1 in Fig. 1c is quite similar to the pattern of duty cycle vs. average ω_1 in supporting information Figure S1c, suggesting that the rotation transfer effect depends mainly on the duty cycle. The MTR_{asym_CW} and $MTR_{asym\_2\pi}$ values directly reflect the measured signal variation due to the CEST/NOE effects. Higher ω_1 or average ω_1 can not only increase the CEST/NOE effects, but reduce the measured signal variation due to the shine-through effect from greater DS and MT effects. These MTR_{asym} metrics can thus be used to optimize ω_1 or average ω_1 for higher SNRs. Fig. 1h shows that the optimized average ω_1 in the 2π-CEST is approximately 1.2μT at 9.4T. For a certain duty cycle, this average ω_1 can be obtained by adjusting τ_s.

Fig. 2 shows the ratio of the $AREX_{asym\_2\pi}$, $AREX_{asym\_CW}$, $MTR_{asym\_2\pi}$, and MTR_{asym_CW} values for amide protons to those for macromolecular protons from the simulated CW-CEST and 2π-CEST signals with varied sequence parameters but constant sample parameters. Notice that the ratio is smaller with a lower duty cycle and shorter τ_s in the 2π-CEST. For example, with a duty cycle of 20% and τ_s of 10ms in the 2π-CEST, the relative contribution from the APT effect to the NOE effect at −3.5ppm is 56.3%. In contrast, in the corresponding CW-CEST, it is 176.2%. This result suggests that the low-duty-cycle 2π-CEST can effectively reduce the contamination from the APT effect to the quantification of the NOE effect at −3.5 ppm.

Fig. 3 shows the simulated $AREX_{asym\_2pi}$, $AREX_{asym\_CW}$, $AREX_{asym\_2pi}/AREX_{asym\_CW}$, MTR_{asym_2pi}, MTR_{asym_CW}, and $MTR_{asym\_2pi}/MTR_{asym\_CW}$ as a function of k_{sw} and T_{2s}, respectively, with other sample parameters kept constant. Compared with $AREX_{asym\_CW}$ and MTR_{asym_CW}, $AREX_{asym\_2pi}$ and MTR_{asym_2pi} are less sensitive to slow-intermediate exchanging pools with relatively long T_{2s} (e.g., amide at 3.5ppm and guanidino amine at 2ppm), but are sensitive to short T_{2s} components with slow k_{sw} (e.g., NOE effect at −3.5ppm) and fast exchanging pools (e.g., lysine amine at 3 ppm). This simulation suggests that 2π-CEST can also remove the guanidino amine at 2ppm in addition to the APT effect but not the lysine amine at 3ppm.

Fig. 4 shows the average CW-CEST and 2π-CEST Z-spectra as well as the $AREX_{asym\_CW}$, $AREX_{asym\_2pi}$, MTR_{asym_CW}, MTR_{asym_2pi}, $AREX_{multifit\_CW}$, and $MTR_{multifit\_CW}$ spectra

from the tumor and the contralateral normal tissue of three rat brains. Note in Fig. 4a that although the APT at 3.5ppm and the guanidino amine at 2ppm are apparent in the CW-CEST spectra, they become weak in the 2π-CEST spectra. Additionally, note in Fig. 4b and 4c that two dips at −3.5 ppm and −2 ppm are overlaid on a broad NOE peak on the $AREX_{asym\_CW}$ and MTR_{asym_CW} spectra, which is due to the contamination from the APT and the guanidino amine, but not on the $AREX_{asym\_2pi}$ and MTR_{asym_2pi} spectra.

Fig. 5 shows the significant differences in the NOE effect at −3.5ppm quantified by $AREX_{asym\_CW}$, $AREX_{asym\_2\pi}$, $AREX_{multifit\_CW}$, MTR_{asym_CW}, $MTR_{asym\_2\pi}$, and $MTR_{multifit\_CW}$ between tumor and contralateral normal tissues in rat brains. All these metrics show significant differences between the tumor and contralateral normal tissue, except for $MTR_{multifit\_CW}$.

Fig. 6 shows the maps of $AREX_{asym\_CW}$ at −3.5ppm, $AREX_{asym\_2\pi}$ at −3.5ppm, $AREX_{asym\_CW}$ at −4.25ppm, and $AREX_{multifit\_CW}$ of NOE from the three rat brains. Fig. 7 shows the maps of MTR_{asym_CW} at −3.5ppm, $MTR_{asym\_2\pi}$ at −3.5ppm, MTR_{asym_CW} at −4.25ppm, and $MTR_{multifit\_CW}$ of NOE from the three rat brains. Since the APT peak is much narrower than the NOE peak at −3.5ppm, $AREX_{asym\_CW}$ and MTR_{asym_CW} at −4.25ppm (subtraction of the label signal at −4.25ppm and the reference signal at 4.25ppm) were used to avoid contamination from the APT effect. Supporting Information Table S3 lists the standard deviation of these values from all voxels in the tumor regions from the three rat brains. Note that the standard deviations from the tumor regions in the maps of $AREX_{asym\_2\pi}$(−3.5ppm) and $MTR_{asym\_2\pi}$(−3.5ppm) are much smaller than those from $AREX_{asym\_CW}$(−3.5ppm) and MTR_{asym_CW}(−3.5ppm) for all the three rats. Also observe that the standard deviations from the tumor regions in the maps of $AREX_{asym\_2\pi}$(−3.5ppm) and $MTR_{asym\_2\pi}$(−3.5ppm) are much smaller than those from $AREX_{asym\_CW}$(−4.25ppm) and MTR_{asym_CW}(−4.25ppm) for the rat #2 and #3, and close to those from $AREX_{asym\_CW}$(−4.25ppm) and MTR_{asym_CW}(−4.25ppm) for the rat #1. This suggests that after removing the confounding APT signals by using the low-duty-cycle 2π-CEST, the NOE imaging in the tumor regions become more homogeneous. The standard deviations from the tumor regions in the maps of $AREX_{asym\_2\pi}$(−3.5ppm) and $MTR_{asym\_2\pi}$(−3.5ppm) are also much smaller than those from $AREX_{multifit\_CW}$ and $MTR_{multifit\_CW}$ of NOE, except for $AREX_{asym\_2\pi}$(−3.5ppm) in rat #1. The dark voxels in some maps are negative values, which are due to the significant contamination from the APT effect. Supporting Information Table S3 also shows the number of voxels with negative values. For rat #2 as an example, the number of voxels with negative values in the $AREX_{asym\_2\pi}$(−3.5ppm) and $MTR_{asym\_2\pi}$(−3.5ppm) maps (2 voxels) as well as maps of $AREX_{multifit\_CW}$ and $MTR_{multifit\_CW}$ of NOE (0 voxel) are much smaller than that in the $AREX_{asym\_CW}$(−4.25ppm) and MTR_{asym_CW}(−4.25ppm) maps (6 voxels) as well as $AREX_{asym\_CW}$(−3.5ppm) and MTR_{asym_CW}(−3.5ppm) maps (13 voxels), suggesting the reduced contamination from the APT effect by using the low-duty-cycle 2π-CEST.

Fig. 8 shows the average multiple-pool Lorentzian fitted APT, amine, NOE, and MT spectra using $AREX_{multifit\_CW}$ and $MTR_{multifit\_CW}$ as well as the average $AREX_{asym\_multifit\_CW}$ and $MTR_{asym\_multifit\_CW}$ spectra for each pool from the tumor and the contralateral normal tissue. Supporting Information Table S4 lists the values of

$AREX_{asym\_multifit\_CW}$ and $MTR_{asym\_multifit\_CW}$ at −3.5ppm from each fitted CEST/NOE pool, $AREX_{asym\_CW}$ and MTR_{asym_CW} at −3.5ppm, as well as $AREX_{asym\_2\pi}$ and $MTR_{asym\_2\pi}$ at −3.5ppm. Note that besides NOE, there are also contributions from APT, amine, and MT asymmetry to $AREX_{asym\_CW}$ and MTR_{asym_CW}. In tumors, the contribution from APT ($AREX_{asym\_multifit\_CW}$ and $MTR_{asym\_multifit\_CW}$ at −3.5ppm for APT are $-0.058\pm0.006s^{-1}$ and −0.058±0.023, respectively) are comparable to that from NOE ($AREX_{asym\_multifit\_CW}$ and $MTR_{asym\_multifit\_CW}$ at −3.5ppm for NOE are $0.089\pm0.012s^{-1}$ and 0.109±0.005, respectively), suggesting the necessity to remove APT. In contrast, contributions from amine ($AREX_{asym\_multifit\_CW}$ and $MTR_{asym\_multifit\_CW}$ at −3.5ppm for amine are $-0.025\pm0.013s^{-1}$ and −0.030±0.014, respectively) and MT asymmetry ($AREX_{asym\_multifit\_CW}$ and $MTR_{asym\_multifit\_CW}$ at −3.5ppm for MT asymmetry are $0.016\pm0.011s^{-1}$ and 0.024±0.017, respectively) are relatively small compared with that from NOE. This suggests that the asymmetric analysis of 2π-CEST can significantly improve the accuracy in quantifying NOE in tumors after removing the contribution from APT. In normal tissues, the contribution from APT, amine, and MT asymmetry are relatively small compared with that from NOE. ($AREX_{asym\_multifit\_CW}$ and $MTR_{asym\_multifit\_CW}$ are $-0.046\pm0.005s^{-1}$ and −0.033±0.011, respectively, for APT, are −0.036±0.014 and −0.036±0.014, respectively for amine, are $0.158\pm0.016s^{-1}$ and 0.114±0.012, respectively, for NOE, as well as are $0.049\pm0.012s^{-1}$ and 0.052±0.009, respectively, for MT asymmetry). Thus our low-duty-cycle 2π-CEST method provides an NOE-weighted imaging with the contribution from NOE dominating other confounding signals.

Fig. 9 shows the measured 2π-CEST Z-spectra on three samples of Egg PC, BSA, and EWA. Note that the NOE effect at −3.5ppm is present in all these samples. This experiment suggests that both phospholipids and proteins may contribute to the NOE effect at −3.5 ppm. Besides the NOE effect at −3.5ppm in Egg PC, the NOE effect at approximately −1.6ppm can also be observed in Egg PC, which is in agreement with our previous reports on both animals and samples of reconstituted phospholipids (16–22).

Fig. 10 gives the simulated $AREX_{asym}$/nominal $AREX_{asym}$ and MTR_{asym}/nominal MTR_{asym} as a function of the B_1 and B_0 shifts. Note that the 2π-CEST is more robust to the B_1 shift than the CW-CEST but is less robust to the B_0 shift than the CW-CEST. In these preclinical experiments, the B_1 and B_0 shifts are very small. However, in situations where the B_1 and B_0 shifts are severe, correction of these field shifts is necessary.

DISCUSSION

In this paper, we used asymmetric analysis of low-duty-cycle 2π-CEST signals to provide a more accurate quantification of the NOE effect at −3.5ppm in tumors by reducing contamination from the APT effect. In normal tissues with commonly used saturation powers (e.g. 1 μT), the NOE effect at −3.5ppm is much larger than the APT effect as shown in supporting information Table S4 as well as our previous reports (18,47), so the resulting contamination from APT can be ignored. However, in tumors with commonly used saturation powers (e.g. 1μT), the NOE effect at −3.5ppm is comparable to the APT effect (18), which produces a complex signal origin in tumors using the conventional asymmetric analysis method. The phantom studies in Fig. 8 show that the NOE effect at −3.5ppm

may arise from both phospholipids and large proteins which have reduced correlation time. Phospholipids have been shown to be cancer biomarkers (60). The concentration of most phospholipid species decreases in tumors, which may contribute to the decreased NOE signal at −3.5ppm quantified by all AREX metrics in tumors. The variation in the structure of large proteins in tumors may also contribute to the decreased NOE effect at −3.5ppm quantified by all AREX metrics in tumors (61). In contrast, APT should mainly arise from mobile proteins/peptides (10), but not large proteins since amide groups inside large proteins might be isolated from water protons and thus should make smaller contributions to APT. These different molecular origin causes the relatively longer T_{2s} for amide, but shorter T_{2s} for NOE, based on which we can separate them by using the 2π-CEST.

APT signal has been traditionally quantified by the asymmetric analysis method, which should have contributions from both APT and NOE based on our analysis in Fig. 8. Previously, both the APT quantified by the asymmetric analysis and NOE have shown clinical interest in diagnosing tumors (10,23,40–45,62–66). It is thus not clear which effect contributes to the diagnosis. Further studies to investigate the clinical interest of specifically quantified APT and NOE are required for optimizing the sequence and for finding the underlying imaging biomarkers.

The contamination from the APT effect decreases the values of the quantified NOE effect at −3.5ppm using the conventional asymmetric analysis method and produces negative values in some voxels (dark voxels) in the tumor regions in Fig. 6 and Fig. 7. This reduces the accuracy and specificity of the quantification of the NOE effect at −3.5ppm, and may cause diagnostic errors. In contrast, the maps of the NOE effect at −3.5ppm obtained using 2π-CEST have nearly no negative values. The use of $AREX_{asym\_CW}$ at −4.25ppm to avoid contamination from the APT effect can also reduce the number of negative values. However, it relies on the choice of the RF offsets and the magnetic fields. The images in Fig. 6 and Fig. 7 suggest that 2π-CEST has better performance than $AREX_{asym\_CW}$ at −4.25ppm in reducing the number of negative values.

The simulations in Fig. 1a, 1b, 1e, and 1f suggest that the 2π-CEST has better signal selectivity for a lower duty cycle. However, a lower duty cycle results in a lower average ω_1 for a certain τ_s. The simulations in Fig. 1h show that the MTR_{asym} values, which reflect the SNR of the signal variation due to the NOE effect, decrease with very low average ω_1 when it is less than the optimal average ω_1. The simulations in Fig. 2a and 2c show that a shorter τ_s results in less contribution from the APT to the NOE effect. However, a shorter τ_s results in a higher average ω_1 for a certain duty cycle. The simulations in Fig. 1h also show that the MTR_{asym} values increase until the optimal average ω_1 is reached. When the ω_1 is higher than the optimal average ω_1, the MTR_{asym} values decrease. In our experiments at 9.4T, we used τ_s of 13ms and duty cycle of 18.1%, corresponding to an average ω_1 of 1μT, which is close to the optimal average ω_1. At lower magnetic fields, the DS effect is more significant and the optimized average ω_1 should be lower. Optimizing the 2π-CEST sequence parameters requires consideration of both the specificity and the sensitivity to the NOE effect at −3.5ppm.

The simulations in Fig. 2 suggest that the relative contribution from the APT effect to the NOE effect at −3.5 ppm by using the 2π-CEST sequence with a duty cycle of 20% and τ_s of 10ms can be reduced by a factor of 3 compared with that using the CW-CEST sequence. In this simulation, the concentrations and exchange rate of the amide and macromolecular protons are the same so that the contribution from only T_{2s} can be observed. In biological tissues, the NOE coupling rate is much slower than the amide-water exchange rate, and the macromolecular concentration should be higher than the amide concentration considering that the amplitude of the NOE effect at 3.5 ppm is usually larger than the APT effect. Supporting Information Figure S2, S3, and S4 show the same simulations to Fig. 1, 2, and 3, respectively, but with f_s of 0.01 and k_{sw} of $15s^{-1}$ for the macromolecular protons (other parameters were not changed). Similar conclusion to that in Fig. 1–3 can be found.

Previously, the contributions to APT signal quantified by the conventional asymmetric analysis in tumors have been also evaluated (67) . Our results are different from this previous paper which shows that the both APT and NOE effects are very small and MT asymmetry dominates the APT signal quantified by the conventional asymmetric analysis. This may be due to that: first, the previous experiment was performed at 3T and used much shorter saturation time, which caused much lower APT signal; second, the previous experiment used a polynomial fitting to quantify NOE. This method requires prior knowledge of the frequency range of the solute peak. By arbitrarily setting this frequency range to be from −2 to −5ppm in this previous paper, it may underestimate the NOE. We have previously compared the accuracy of the multiple-pool Lorentzian fit in quantifying CEST/NOE with a few other quantification methods, which suggested that the multiple-pool Lorentzian fit with low ω_1 is more accurate than other methods (47). In addition, the $MTR_{asym\_multifit\_CW}$ at 10ppm from normal tissue in Fig. 8d is ~0.057 which is in agreement with another previous report in quantifying MT asymmetry at 9.4T (68); lastly, the previous experiment as well as all MTR metrics in our paper used the direct subtraction of label and reference signals which have contaminations from MT, DS, and T_1. Since MT and T_1 change significantly in tumor, these MTR metrics cannot specifically reflect the actual change in the solute of interest. In contrast, the AREX metrics provide specific quantification of solute of interest.

A recent study shows the presence of downfield aromatic NOE which overlaps with APT (69). Based on our simulations in Fig. 3d, if the T_{2s} of aromatic protons is as long as that of amide protons, the low-duty-cycle 2π-CEST can also reduce its contribution. If the T_{2s} of aromatic protons is much shorter than that of amide protons, it should have a broader peak than APT. Then the multiple-pool Lorentzian fitted amine should contain the additional contribution from the aromatic NOE. However, this should be also a small contribution based on the fitted values shown in supporting information Table S4.

In Fig. 1c, the average ω_1 was varied by changing the duty cycle and τ_s, but keeping the saturation pulse flip angle constant, to study the dependence of the rotation effect on duty cycle. In Fig. 9a, the average ω_1 was varied by changing the saturation pulse flip angle, but keeping the duty cycle and τ_s constant, to study the dependence of the 2π-CEST signal on B_1 inhomogeneity. Different dependence of $AREX_{asym}$ on the average ω_1 in Fig. 1c and Fig. 9a were found. This is due to that the pulsed-CEST signal has a complex dependence on not only the average ω_1 but multiple other sequence parameters (48).

CONCLUSION

The NOE effect at −3.5ppm reflects important macromolecules (i.e., phospholipids and proteins) in tissues that are associated with multiple pathologies. 2π-CEST can provide a more accurate and specific quantification of the NOE effect at −3.5ppm by reducing the contamination from the APT effect. In tumors where the NOE effect at −3.5ppm is comparable to the APT effect, the 2π-CEST imaging of the NOE effect at −3.5ppm shows significant advantages over the conventional asymmetric analysis method.

Supplementary Material

Refer to Web version on PubMed Central for supplementary material.

Grant Sponsor:

R21 AR074261, R03 EB029078, R01 EB029443

REFERENCES

1. Zhou JY, van Zijl PCM. Chemical exchange saturation transfer imaging and spectroscopy. Prog Nucl Mag Res Sp 2006;48(2–3):109–136.
2. van Zijl PCM, Yadav NN. Chemical Exchange Saturation Transfer (CEST): What is in a Name and What Isn't? Magnetic Resonance In Medicine 2011;65(4):927–948. [PubMed: 21337419]
3. Kim J, Wu Y, Guo Y, Zheng H, Sun PZ. A review of optimization and quantification techniques for chemical exchange saturation transfer MRI toward sensitive in vivo imaging. Contrast media & molecular imaging 2015;10(3):163–178. [PubMed: 25641791]
4. Wu B, Warnock G, Zaiss M, Lin C, Chen M, Zhou Z, Mu L, Nanz D, Tuura R, Delso G. An overview of CEST MRI for non-MR physicists. Ejnmmi Phys 2016;3(1).
5. van Zijl PCM, Lam WW, Xu JD, Knutsson L, Stanisz GJ. Magnetization Transfer Contrast and Chemical Exchange Saturation Transfer MRI. Features and analysis of the field-dependent saturation spectrum. Neuroimage 2018;168:222–241. [PubMed: 28435103]
6. Anderson WA, Freeman R. Influence Of a Second Radiofrequency Field on High-Resolution Nuclear Magnetic Resonance Spectra. J Chem Phys 1962;37(1):85–&.
7. Vogeli B The nuclear Overhauser effect from a quantitative perspective. Progress in Nuclear Magnetic Resonance Spectroscopy 2014;78:1–46. [PubMed: 24534087]
8. Solomon I Relaxation Processes In a System Of 2 Spins. Phys Rev 1955;99(2):559–565.
9. Wolff SD, Balaban RS. Nmr Imaging Of Labile Proton-Exchange. Journal Of Magnetic Resonance 1990;86(1):164–169.
10. Zhou JY, Tryggestad E, Wen ZB, Lal B, Zhou TT, Grossman R, Wang SL, Yan K, Fu DX, Ford E, Tyler B, Blakeley J, Laterra J, van Zijl PCM. Differentiation between glioma and radiation necrosis using molecular magnetic resonance imaging of endogenous proteins and peptides. Nature medicine 2011;17(1):130–U308.
11. Zhou J, Payen JF, Wilson DA, Traystman RJ, van Zijl PC. Using the amide proton signals of intracellular proteins and peptides to detect pH effects in MRI. Nature medicine 2003;9(8):1085–1090.
12. Cai K, Haris M, Singh A, Kogan F, Greenberg JH, Hariharan H, Detre JA, Reddy R. Magnetic resonance imaging of glutamate. Nature medicine 2012;18(2):302–306.
13. Haris M, Nanga RPR, Singh A, Cai K, Kogan F, Hariharan H, Reddy R. Exchange rates of creatine kinase metabolites: feasibility of imaging creatine by chemical exchange saturation transfer MRI. NMR in biomedicine 2012;25(11):1305–1309. [PubMed: 22431193]
14. Haris M, Singh A, Cai KJ, Kogan F, McGarvey J, DeBrosse C, Zsido GA, Witschey WRT, Koomalsingh K, Pilla JJ, Chirinos JA, Ferrari VA, Gorman JH, Hariharan H, Gorman RC, Reddy

R. A technique for in vivo mapping of myocardial creatine kinase metabolism. Nature medicine 2014;20(2):209–214.

15. Cai K, Singh A, Poptani H, Li W, Yang S, Lu Y, Hariharan H, Zhou XJ, Reddy R. CEST signal at 2ppm (CEST@2ppm) from Z-spectral fitting correlates with creatine distribution in brain tumor. NMR in biomedicine 2015;28(1):1–8. [PubMed: 25295758]
16. Zhang XY, Wang F, Afzal A, Xu JZ, Gore JC, Gochberg DF, Zu ZL. A new NOE-mediated MT signal at around-1.6 ppm for detecting ischemic stroke in rat brain. Magn Reson Imaging 2016;34(8):1100–1106. [PubMed: 27211260]
17. Zhang XY, Wang F, Jin T, Xu JZ, Xie JP, Gochberg DF, Gore JC, Zu ZL. MR imaging of a novel NOE-mediated magnetization transfer with water in rat brain at 9.4T. Magnetic Resonance In Medicine 2017;78(2):588–597. [PubMed: 27604612]
18. Zu ZL. Ratiometric NOE(−1.6) contrast in brain tumors. NMR in biomedicine 2018;31(12).
19. Zu ZL. Toward more reliable measurements of NOE effects in CEST spectra at around-1.6 ppm (NOE (−1.6)) in rat brain. Magnetic Resonance In Medicine 2019;81(1):208–219. [PubMed: 30058128]
20. Cui J, Zhao Y, Wang F, Gochberg DF, Zu ZL. Contribution of blood to nuclear Overhauser effect at-1.6 ppm. Magnetic Resonance In Medicine 2022;87(1):409–416. [PubMed: 34480767]
21. Zaiss M, Schuppert M, Deshmane A, Herz K, Ehses P, Fullbier L, Lindig T, Bender B, Ernemann U, Scheffler K. Chemical exchange saturation transfer MRI contrast in the human brain at 9.4 T. Neuroimage 2018;179:144–155. [PubMed: 29894826]
22. Shah SM, Mougin OE, Carradus AJ, Geades N, Dury R, Morley W, Gowland PA. The z-spectrum from human blood at 7T. Neuroimage 2018;167:31–40. [PubMed: 29111410]
23. Jones CK, Huang A, Xu JD, Edden RAE, Schar M, Hua J, Oskolkov N, Zaca D, Zhou JY, McMahon MT, Pillai JJ, van Zijl PCM. Nuclear Overhauser enhancement (NOE) imaging in the human brain at 7 T. Neuroimage 2013;77(0):114–124. [PubMed: 23567889]
24. Liu DP, Zhou JY, Xue R, Zuo ZT, An J, Wang DJJ. Quantitative Characterization of Nuclear Overhauser Enhancement and Amide Proton Transfer Effects in the Human Brain at 7 Tesla. Magnetic Resonance In Medicine 2013;70(4):1070–1081. [PubMed: 23238951]
25. Yan K, Fu ZM, Yang C, Zhang K, Jiang SS, Lee DH, Heo HY, Zhang Y, Cole RN, Van Eyk JE, Zhou JY. Assessing Amide Proton Transfer (APT) MRI Contrast Origins in 9 L Gliosarcoma in the Rat Brain Using Proteomic Analysis. Mol Imaging Biol 2015;17(4):479–487. [PubMed: 25622812]
26. Chen L, Zeng HF, Xu X, Yadav NN, Cai SH, Puts NA, Barker PB, Li T, Weiss RG, van Zijl PCM, Xu JD. Investigation of the contribution of total creatine to the CEST Z-spectrum of brain using a knockout mouse model. NMR in biomedicine 2017;30(12).
27. Zhang XY, Xie JP, Wang F, Lin EC, Xu JZ, Gochberg DF, Gore JC, Zu ZL. Assignment of the molecular origins of CEST signals at 2ppm in rat brain. Magnetic Resonance In Medicine 2017;78(3):881–887. [PubMed: 28653349]
28. Chen L, Barker PB, Weiss RG, van Zijl PCM, Xu JD. Creatine and phosphocreatine mapping of mouse skeletal muscle by a polynomial and Lorentzian line-shape fitting CEST method. Magnetic Resonance In Medicine 2019;81(1):69–78. [PubMed: 30246265]
29. Chen L, Schar M, Chan KWY, Huang JP, Wei ZL, Lu HZ, Qin Q, Weiss RG, van Zijl PCM, Xu JD. In vivo imaging of phosphocreatine with artificial neural networks. Nat Commun 2020;11(1).
30. Crescenzi R, DeBrosse C, Nanga RPR, Reddy S, Haris M, Hariharan H, Iba M, Lee VMY, Detre JA, Borthakur A, Reddy R. In vivo measurement of glutamate loss is associated with synapse loss in a mouse model of tauopathy. Neuroimage 2014;101:185–192. [PubMed: 25003815]
31. Haris M, Nath K, Cai KJ, Singh A, Crescenzi R, Kogan F, Verma G, Reddy S, Hariharan H, Melhem ER, Reddy R. Imaging of glutamate neurotransmitter alterations in Alzheimer's disease. NMR in biomedicine 2013;26(4):386–391. [PubMed: 23045158]
32. Davis KA, Nanga RP, Das S, Chen SH, Hadar PN, Pollard JR, Lucas TH, Shinohara RT, Litt B, Hariharan H, Elliott MA, Detre JA, Reddy R. Glutamate imaging (GluCEST) lateralizes epileptic foci in nonlesional temporal lobe epilepsy. Sci Transl Med 2015;7(309):309ra161.
33. Cui J, Zu ZL. Towards the molecular origin of glutamate CEST (GluCEST) imaging in rat brain. Magnetic Resonance In Medicine 2020;83(4):1405–1417. [PubMed: 31691367]

34. Zong XP, Wang P, Kim SG, Jin T. Sensitivity and Source of Amine-Proton Exchange and Amide-Proton Transfer Magnetic Resonance Imaging in Cerebral Ischemia. Magnetic Resonance In Medicine 2014;71(1):118–132. [PubMed: 23401310]
35. van Zijl PCM, Zhou J, Mori N, Payen JF, Wilson D, Mori S. Mechanism of magnetization transfer during on-resonance water saturation. A new approach to detect mobile proteins, peptides, and lipids. Magnetic Resonance In Medicine 2003;49(3):440–449. [PubMed: 12594746]
36. Mori S, Eleff SM, Pilatus U, Mori N, van Zijl PCM. Proton NMR spectroscopy of solvent-saturable resonances: A new approach to study pH effects in situ. Magnetic Resonance In Medicine 1998;40(1):36–42. [PubMed: 9660550]
37. Zu Z, Lin EC, Louie EA, Jiang X, Lankford CL, Damon B, Does MD, Gore JC, Gochberg DF. Chemical exchange rotation transfer imaging of phosphocreatine in muscle. NMR in biomedicine 2020:e4437. [PubMed: 33283945]
38. Wang F, Takahashi K, Li H, Zu ZL, Li K, Xu JZ, Harris RC, Takahashi T, Gore JC. Assessment of unilateral ureter obstruction with multi-parametric MRI. Magnetic Resonance In Medicine 2018;79(4):2216–2227. [PubMed: 28736875]
39. Wang F, Zu ZL, Wu TL, Yan XQ, Lu M, Yang PF, Byun NE, Reed JL, Gore JC, Chen LM. Sensitivity and specificity of CEST and NOE MRI in injured spinal cord in monkeys. Neuroimage-Clin 2021;30.
40. Zaiss M, Kunz P, Goerke S, Radbruch A, Bachert P. MR imaging of protein folding in vitro employing Nuclear-Overhauser-mediated saturation transfer. NMR in biomedicine 2013;26(12):1815–1822. [PubMed: 24115020]
41. Paech D, Zaiss M, Meissner JE, Windschuh J, Wiestler B, Bachert P, Neumann JO, Kickingereder P, Schlemmer HP, Wick W, Nagel AM, Heiland S, Ladd ME, Bendszus M, Radbruch A. Nuclear Overhauser Enhancement Mediated Chemical Exchange Saturation Transfer Imaging at 7 Tesla in Glioblastoma Patients. Plos One 2014;9(8).
42. Mehrabian H, Desmond KL, Soliman H, Sahgal A, Stanisz GJ. Differentiation between Radiation Necrosis and Tumor Progression Using Chemical Exchange Saturation Transfer. Clin Cancer Res 2017;23(14):3667–3675. [PubMed: 28096269]
43. Tang XY, Dai ZZ, Xiao G, Yan G, Shen ZW, Zhang T, Zhang GS, Zhuang ZR, Shen YY, Zhang ZY, Hu W, Wu RH. Nuclear Overhauser Enhancement-Mediated Magnetization Transfer Imaging in Glioma with Different Progression at 7 T. Acs Chem Neurosci 2017;8(1):60–66. [PubMed: 27792315]
44. Lee DH, Heo HY, Zhang K, Zhang Y, Jiang SS, Zhao XN, Zhou JY. Quantitative assessment of the effects of water proton concentration and water T-1 changes on amide proton transfer (APT) and nuclear overhauser enhancement (NOE) MRI: The origin of the APT imaging signal in brain tumor. Magnetic Resonance In Medicine 2017;77(2):855–863. [PubMed: 26841096]
45. Wu YL, Wood TC, Arzanforoosh F, Hernandez-Tamames JA, Barker GJ, Smits M, Warnert EA. 3D APT and NOE CEST-MRI of healthy volunteers and patients with non-enhancing glioma at 3 T. Magn Reson Mater Phy 2022;35(1):63–73.
46. Xu JZ, Zaiss M, Zu ZL, Li H, Xie JP, Gochberg DF, Bachert P, Gore JC. On the origins of chemical exchange saturation transfer (CEST) contrast in tumors at 9.4 T. NMR in biomedicine 2014;27(4):406–416. [PubMed: 24474497]
47. Zhang XY, Wang F, Li H, Xu JZ, Gochberg DF, Gore JC, Zu ZL. Accuracy in the quantification of chemical exchange saturation transfer (CEST) and relayed nuclear Overhauser enhancement (rNOE) saturation transfer effects. NMR in biomedicine 2017;30(7).
48. Zu Z, Li K, Janve VA, Does MD, Gochberg DF. Optimizing pulsed-chemical exchange saturation transfer imaging sequences. Magnetic Resonance in Medicine 2011;66(4):1100–1108. [PubMed: 21432903]
49. Zu ZL, Janve VA, Xu JZ, Does MD, Gore JC, Gochberg DF. A new method for detecting exchanging amide protons using chemical exchange rotation transfer. Magnetic Resonance In Medicine 2013;69(3):637–647. [PubMed: 22505325]
50. Zu Z, Janve VA, Li K, Does MD, Gore JC, Gochberg DF. Multi-angle ratiometric approach to measure chemical exchange in amide proton transfer imaging. Magnetic Resonance in Medicine 2012;68(3):711–719. [PubMed: 22161770]

51. Zu ZL, Xu JZ, Li H, Chekmenev EY, Quarles CC, Does MD, Gore JC, Gochberg DF. Imaging Amide Proton Transfer and Nuclear Overhauser Enhancement Using Chemical Exchange Rotation Transfer (CERT). Magnetic Resonance In Medicine 2014;72(2):471–476. [PubMed: 24302497]
52. Zu ZL, Li H, Xu JZ, Zhang XY, Zaiss M, Li K, Does MD, Gore JC, Gochberg DF. Measurement of APT using a combined CERT-AREX approach with varying duty cycles. Magn Reson Imaging 2017;42:22–31. [PubMed: 28526431]
53. Zu ZL, Louie EA, Lin EC, Jiang XY, Does MD, Gore JC, Gochberg DF. Chemical exchange rotation transfer imaging of intermediate-exchanging amines at 2 ppm. NMR in biomedicine 2017;30(10).
54. Zu ZL, Lin EC, Louie EA, Xu JZ, Li H, Xie JP, Lankford CL, Chekmenev EY, Swanson SD, Does MD, Gore JC, Gochberg DF. Relayed nuclear Overhauser enhancement sensitivity to membrane Cho phospholipids. Magnetic Resonance In Medicine 2020.
55. Zaiss M, Bachert P. Exchange-dependent relaxation in the rotating frame for slow and intermediate exchange - modeling off-resonant spin-lock and chemical exchange saturation transfer. NMR in biomedicine 2013;26(5):507–518. [PubMed: 23281186]
56. Zaiss M, Zu ZL, Xu JZ, Schuenke P, Gochberg DF, Gore JC, Ladd ME, Bachert P. A combined analytical solution for chemical exchange saturation transfer and semi-solid magnetization transfer. NMR in biomedicine 2015;28(2):217–230. [PubMed: 25504828]
57. Hua J, Jones CK, Blakeley J, Smith SA, van Zijl PCM, Zhou JY. Quantitative description of the asymmetry in magnetization transfer effects around the water resonance in the human brain. Magnetic Resonance In Medicine 2007;58(4):786–793. [PubMed: 17899597]
58. Zaiss M, Schmitt B, Bachert P. Quantitative separation of CEST effect from magnetization transfer and spillover effects by Lorentzian-line-fit analysis of z-spectra. Journal of Magnetic Resonance 2011;211(2):149–155. [PubMed: 21641247]
59. Gochberg DF, Gore JC. Quantitative magnetization transfer imaging via selective inversion recovery with short repetition times. Magnetic Resonance in Medicine 2007;57(2):437–441. [PubMed: 17260381]
60. Bandu R, Mok HJ, Kim KP. Phospholipids as Cancer Biomarkers: Mass Spectrometry-Based Analysis. Mass Spectrom Rev 2018;37(2):107–138. [PubMed: 27276657]
61. Goerke S, Zaiss M, Kunz P, Klika KD, Windschuh JD, Mogk A, Bukau B, Ladd ME, Bachert P. Signature of protein unfolding in chemical exchange saturation transfer imaging. NMR in biomedicine 2015;28(7):906–913. [PubMed: 26010522]
62. Jiang SS, Rui QH, Wang Y, Heo HY, Zou TY, Yu H, Zhang Y, Wang XL, Du YX, Wen XR, Chen FY, Wang JH, Eberhart CG, Zhou JY, Wen ZB. Discriminating MGMT promoter methylation status in patients with glioblastoma employing amide proton transfer-weighted MRI metrics. Eur Radiol 2018;28(5):2115–2123. [PubMed: 29234914]
63. Jiang SS, Zou TY, Eberhart CG, Villalobos MAV, Heo HY, Zhang Y, Wang Y, Wang XL, Yu H, Du YX, van Zijl PCM, Wen ZB, Zhou JY. Predicting IDH mutation status in grade II gliomas using amide proton transfer-weighted (APTw) MRI. Magnetic Resonance In Medicine 2017;78(3):1100–1109. [PubMed: 28714279]
64. Jiang SS, Eberhart CG, Zhang Y, Heo HY, Wen ZB, Blair L, Qin HM, Lim M, Quinones-Hinojosa A, Weingart JD, Barker PB, Pomper MG, Laterra J, van Zijl PCM, Blakeley JO, Zhou JY. Amide proton transfer-weighted magnetic resonance image-guided stereotactic biopsy in patients with newly diagnosed gliomas. Eur J Cancer 2017;83:9–18. [PubMed: 28704644]
65. Jiang SS, Eberhart CG, Lim M, Heo HY, Zhang Y, Blair L, Wen ZB, Holdhoff M, Lin D, Huang P, Qin HM, Quinones-Hinojosa A, Weingart JD, Barker PB, Pomper MG, Laterra J, van Zijl PCM, Blakeley JO, Zhou JY. Identifying Recurrent Malignant Glioma after Treatment Using Amide Proton Transfer-Weighted MR Imaging: A Validation Study with Image-Guided Stereotactic Biopsy. Clin Cancer Res 2019;25(2):552–561. [PubMed: 30366937]
66. Yu H, Wen XR, Wu PP, Chen YQ, Zou TY, Wang XL, Jiang SS, Zhou JY, Wen ZB. Can amide proton transfer-weighted imaging differentiate tumor grade and predict Ki-67 proliferation status of meningioma? Eur Radiol 2019;29(10):5298–5306. [PubMed: 30887206]

67. Scheidegger R, Wong ET, Alsop DC. Contributors to contrast between glioma and brain tissue in chemical exchange saturation transfer sensitive imaging at 3 Tesla. Neuroimage 2014;99:256–268. [PubMed: 24857712]

68. Jin T, Kim SG. Advantages of chemical exchange-sensitive spin-lock (CESL) over chemical exchange saturation transfer (CEST) for hydroxyl- and amine-water proton exchange studies. NMR in biomedicine 2014;27(11):1313–1324. [PubMed: 25199631]

69. Jin T, Kim SG. Role of chemical exchange on the relayed nuclear Overhauser enhancement signal in saturation transfer MRI. Magnetic Resonance In Medicine 2022;87(1):365–376. [PubMed: 34382694]

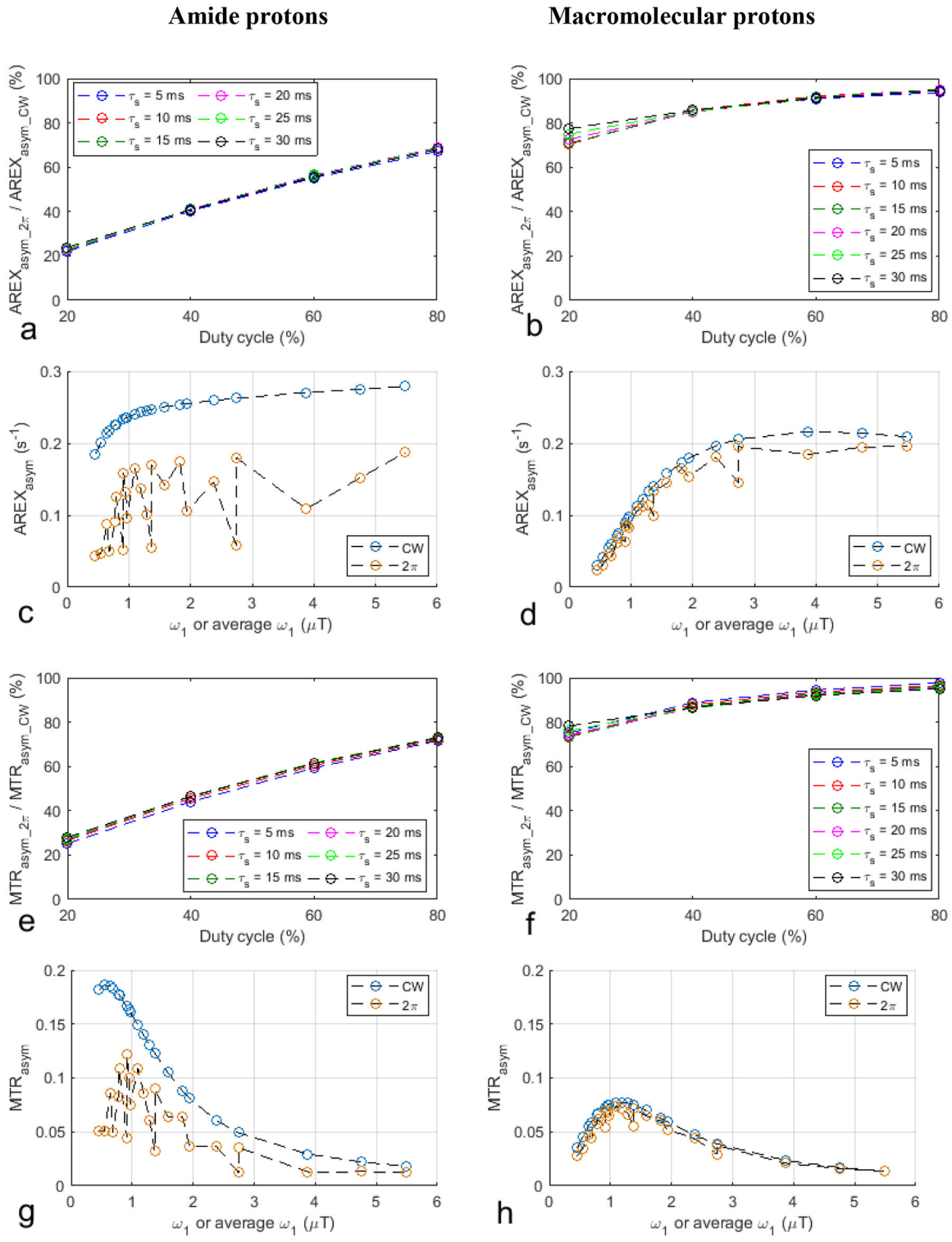

Fig. 1.

Simulated $AREX_{asym\_2\pi}/AREX_{asym\_CW}$ and $MTR_{asym\_2\pi}/MTR_{asym\_CW}$ as a function of duty cycle for a series of τ_s values for amide protons (a, e) and macromolecular protons (b, f). Scatter plot of all the $AREX_{asym\_CW}$, $AREX_{asym\_2\pi}$, MTR_{asym_CW}, and $MTR_{asym\_2\pi}$

values from (a, e, b, f) as a function of ω_1 or average ω_1 for amide protons (c, d) and macromolecular protons (g, h). The CW-CEST signals were simulated with ω_1 the same as the average ω_1 calculated from the duty cycle and pulse duration in the corresponding 2π-CEST. The change of the average ω_1 in the 2π-CEST is obtained by varying the duty cycle and pulse duration. The number of pulses was also adjusted in the 2π-CEST so that T_{sat} was kept at around 5s.

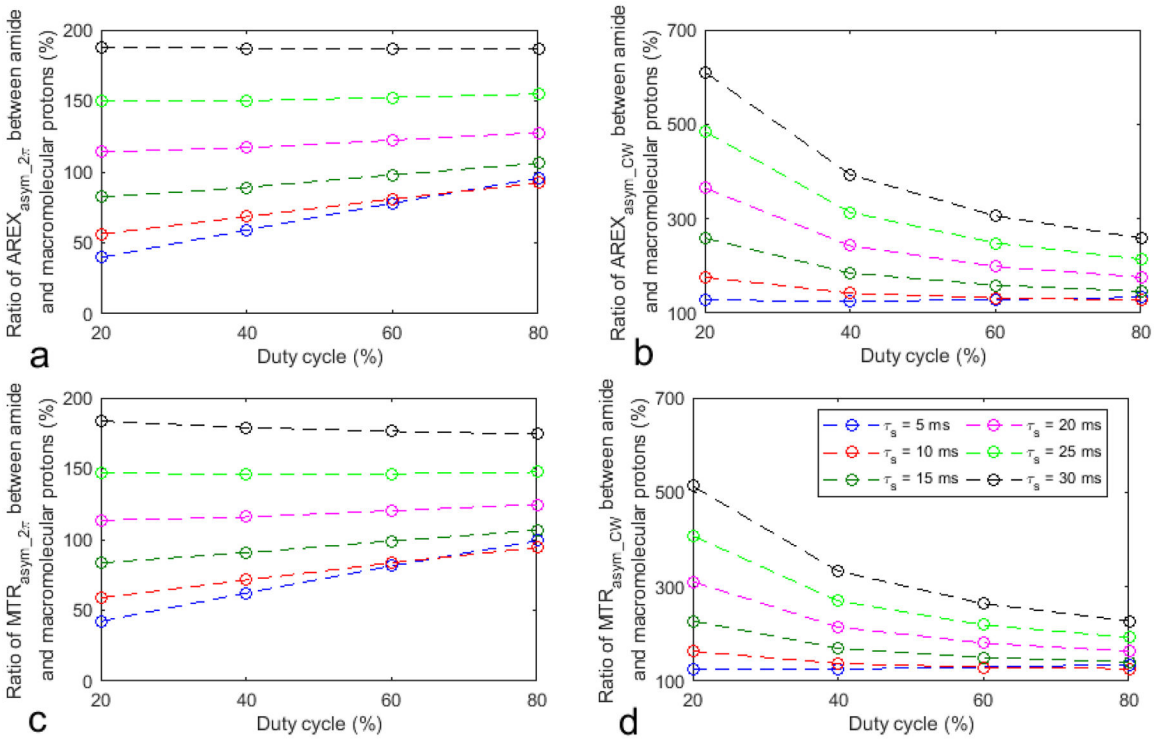

Fig. 2.

Simulated ratio of the $AREX_{asym\_2\pi}$ (a), $AREX_{asym\_CW}$ (b), $MTR_{asym\_2\pi}$ (c), and MTR_{asym_CW} (d) values for amide protons to those for macromolecular protons.

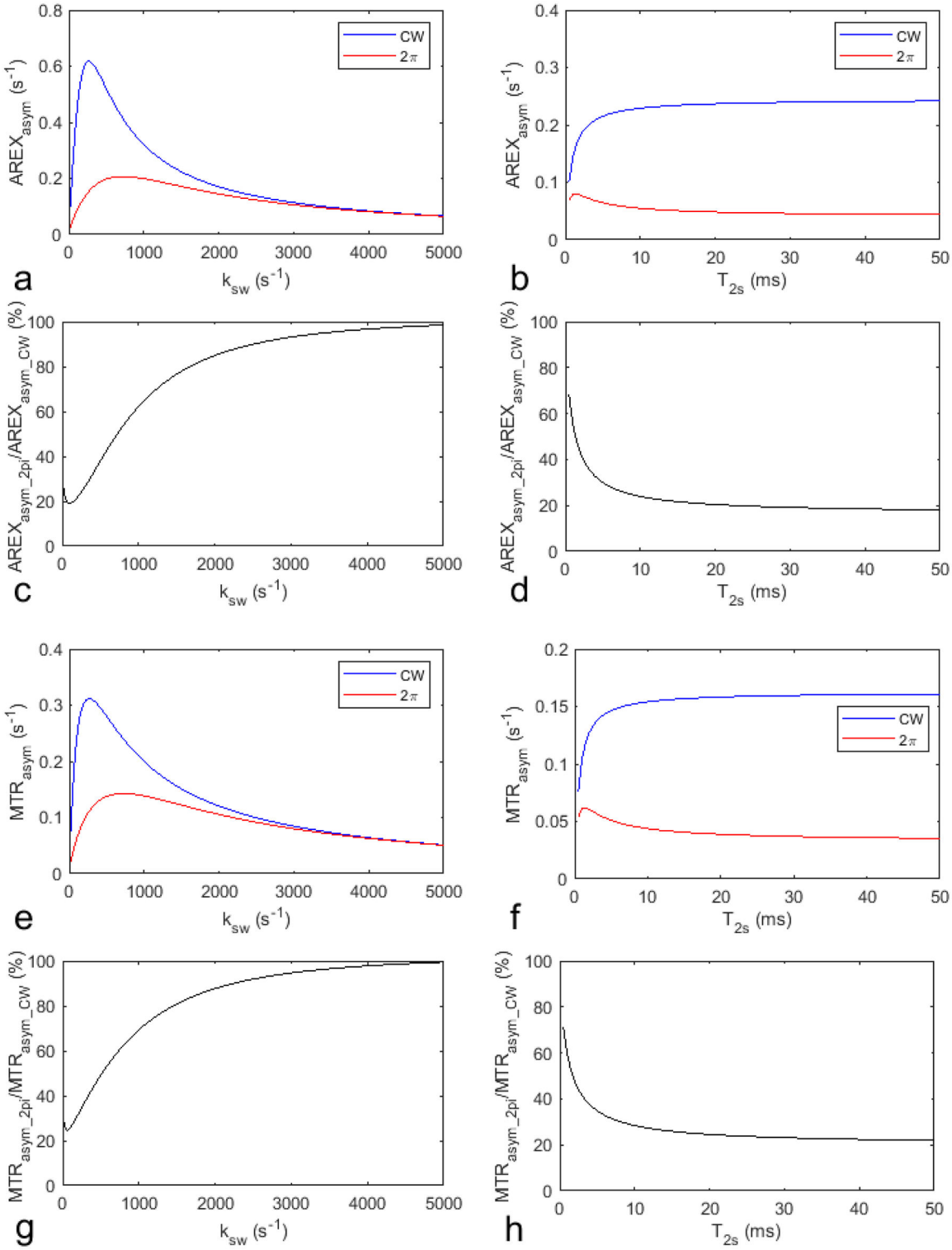

Fig. 3.

Simulated $AREX_{asym\_CW}$ and $AREX_{asym\_2pi}$ values as well as MTR_{asym_CW} and MTR_{asym_2pi} values as a function of k_{sw} (a, e) and T_{2s} (b, f), respectively. Simulated

$AREX_{asym\_2pi}/AREX_{asym\_CW}$ and $MTR_{asym\_2pi}/MTR_{asym\_CW}$ as a function of k_{sw} (c, d) and T_{2s} (g, h), respectively. Other sample parameters were kept constant.

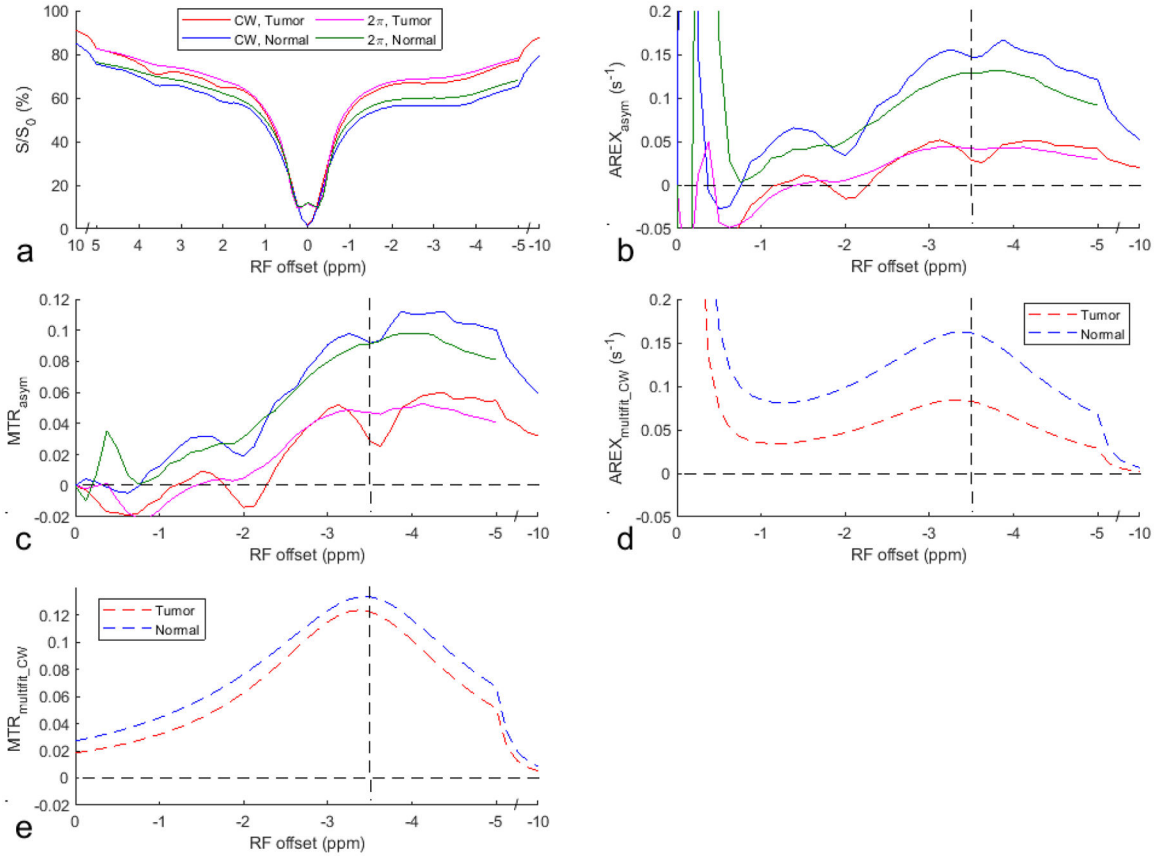

Fig. 4.

Average CW-CEST and 2π-CEST Z-spectra (a), $AREX_{asym\_CW}$ and $AREX_{asym\_2pi}$ spectra (b), MTR_{asym_CW} and MTR_{asym_2pi} spectra (c), $AREX_{multifit\_CW}$ spectra (d), and $MTR_{multifit\_CW}$ spectra (e) from the tumor and the contralateral normal tissue of three rat brains. The vertical dashed line in (b-e) indicates a Δω of −3.5 ppm. The horizontal dashed line in (b-e) indicates the $AREX_{asym}$ and MTR_{asym} values of 0.

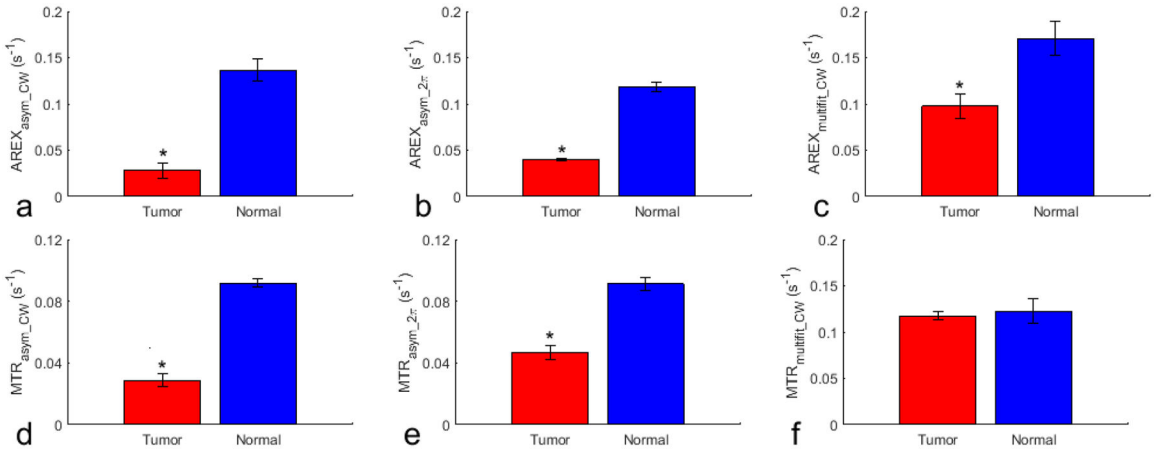

Fig. 5.

Statistical differences in the NOE at −3.5 ppm quantified by $AREX_{asym\_CW}$ (a), $AREX_{asym\_2\pi}$ (b), $AREX_{multifit\_CW}$ (c), MTR_{asym_CW} (d), $MTR_{asym\_2\pi}$ (e), and $MTR_{multifit\_CW}$ (f) between tumor and contralateral normal tissues in the rat brain. (N=3, *P<0.05)

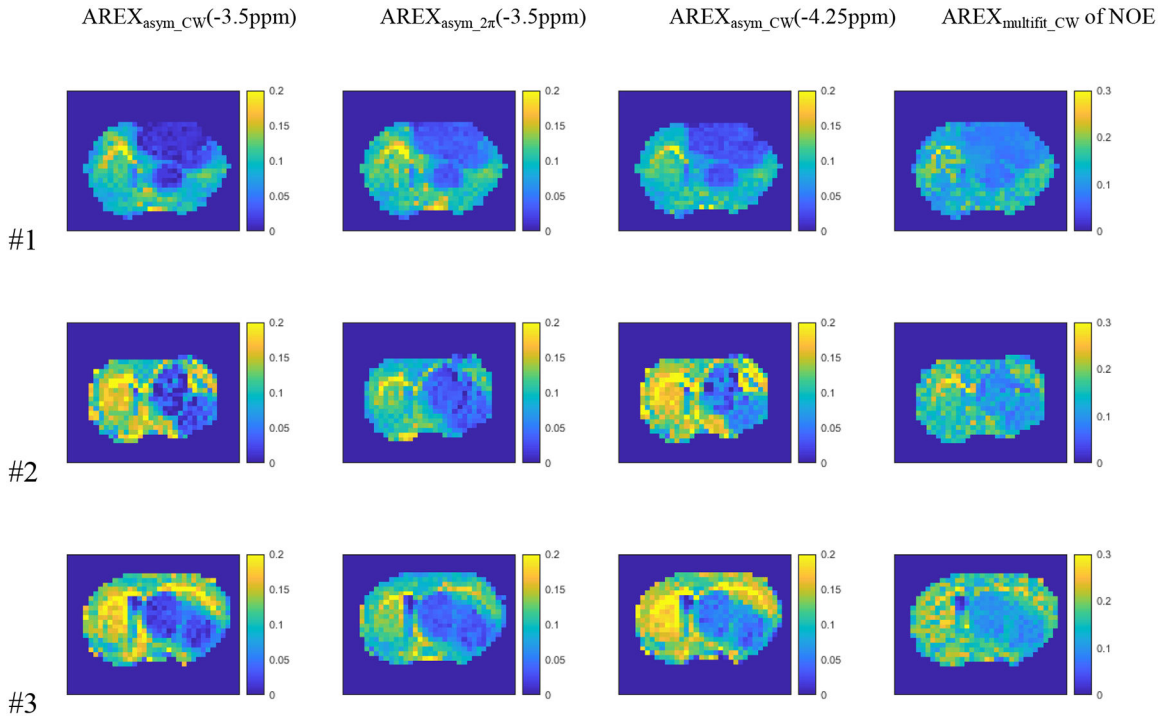

Fig. 6.

Maps of AREX$_{asym_CW}$(−3.5ppm), AREX$_{asym_2pi}$(−3.5ppm), AREX$_{asym_CW}$(−4.25ppm) and AREX$_{multifit_CW}$ of NOE from three rat brains. The units in these figures are s^{-1}.

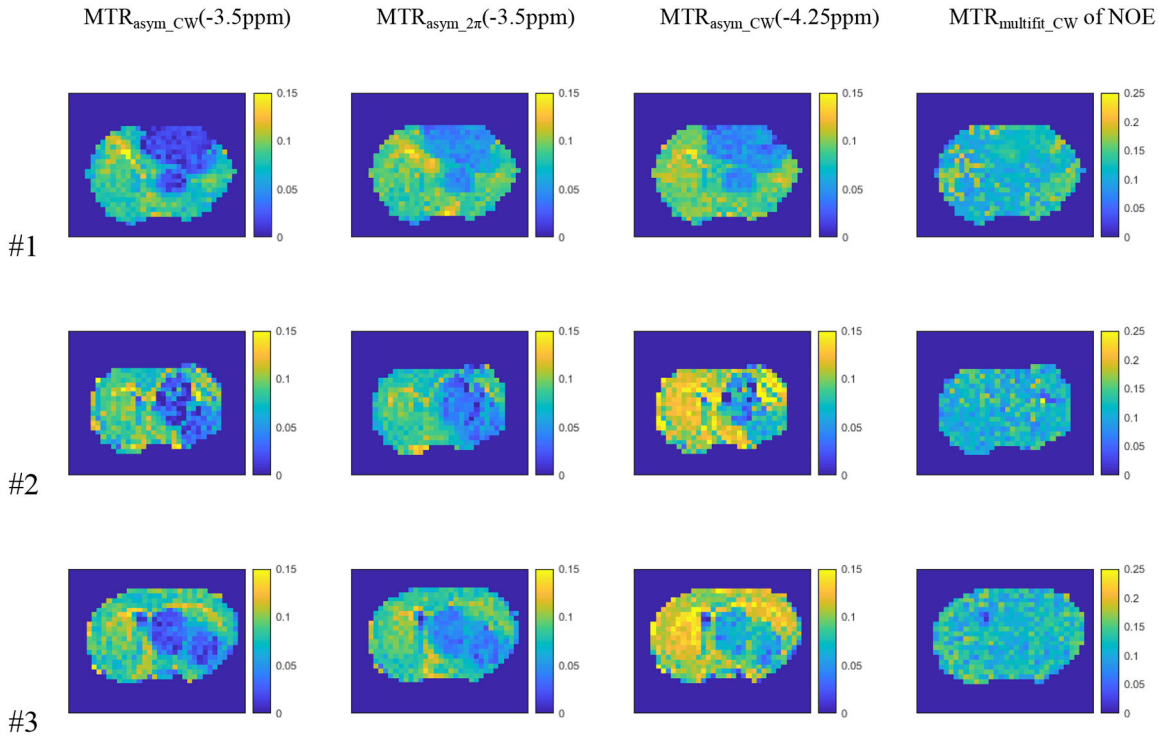

Fig. 7.

Maps of MTR$_{asym_CW}$(−3.5ppm), MTR$_{asym_2pi}$(−3.5ppm), MTR$_{asym_CW}$(−4.25ppm) and MTR$_{multifit_CW}$ of NOE from three rat brains.

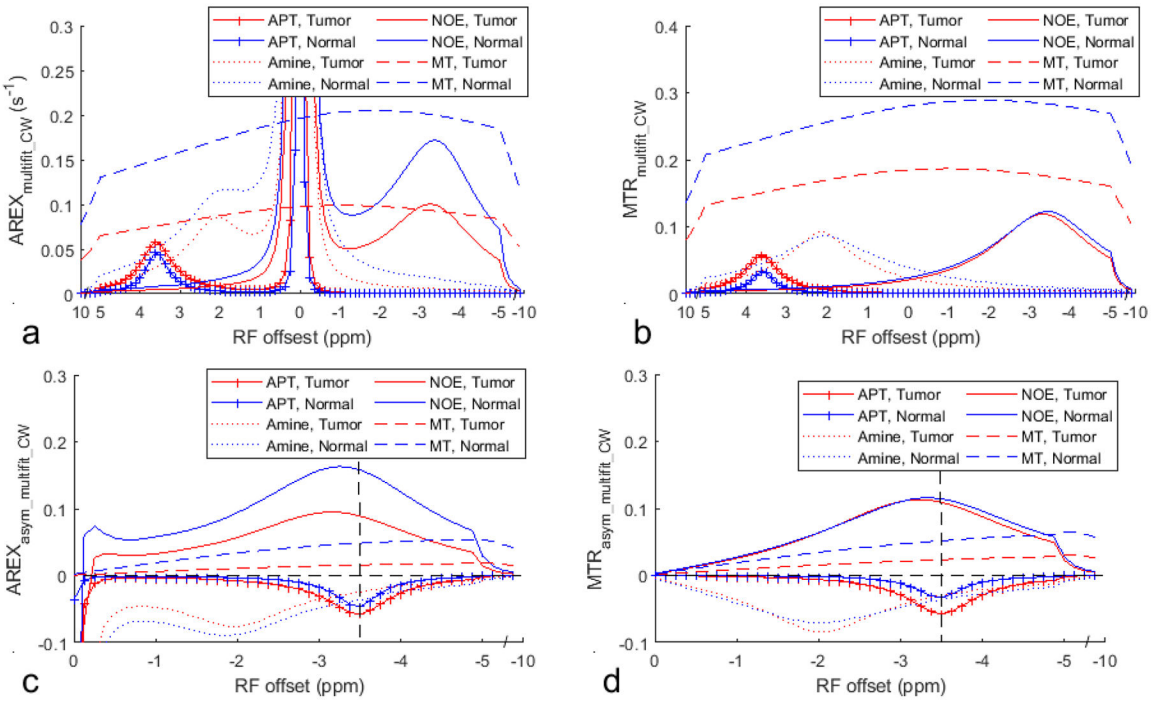

Fig. 8.

Average multiple-pool Lorentzian fitted APT, amine, NOE, and MT spectra using $AREX_{multifit\_CW}$ (a) and $MTR_{multifit\_CW}$ (b), as well as using $AREX_{asym\_multifit\_CW}$ (c) and $MTR_{asym\_multifit\_CW}$ (d) from the tumor and the contralateral normal tissue of three rat brains. The vertical dashed line in (c, d) indicates a Δω of −3.5 ppm. The horizontal dashed line in (c, d) indicates the $AREX_{asym\_CW}$ and MTR_{asym_CW} values of 0.

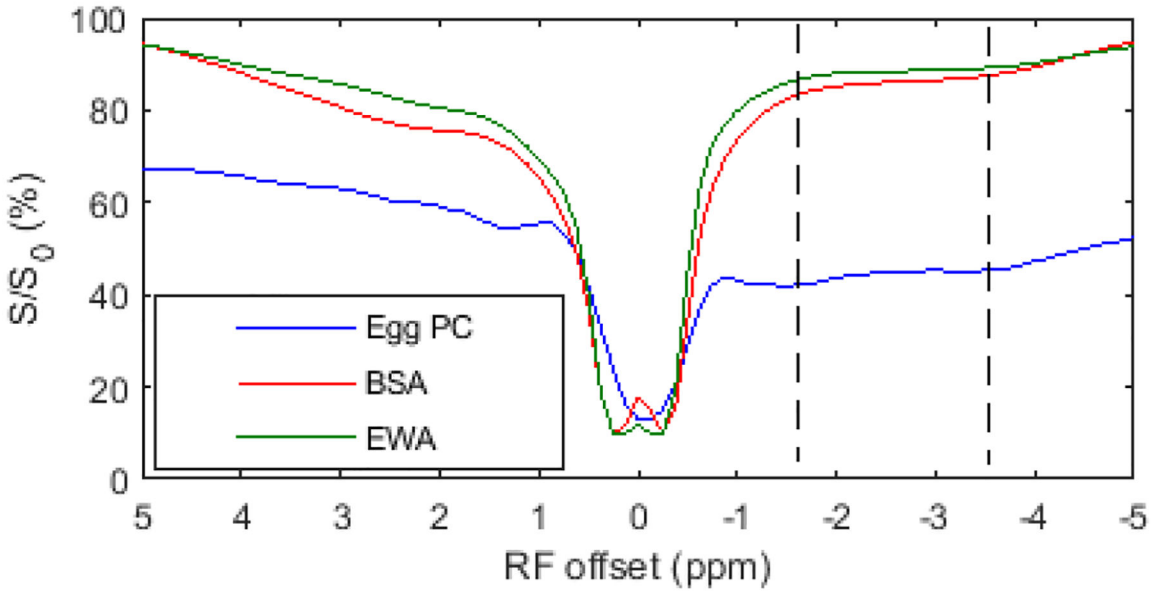

Fig. 9.
2π-CEST Z-spectra on samples of Egg PC, BSA, and EWA.

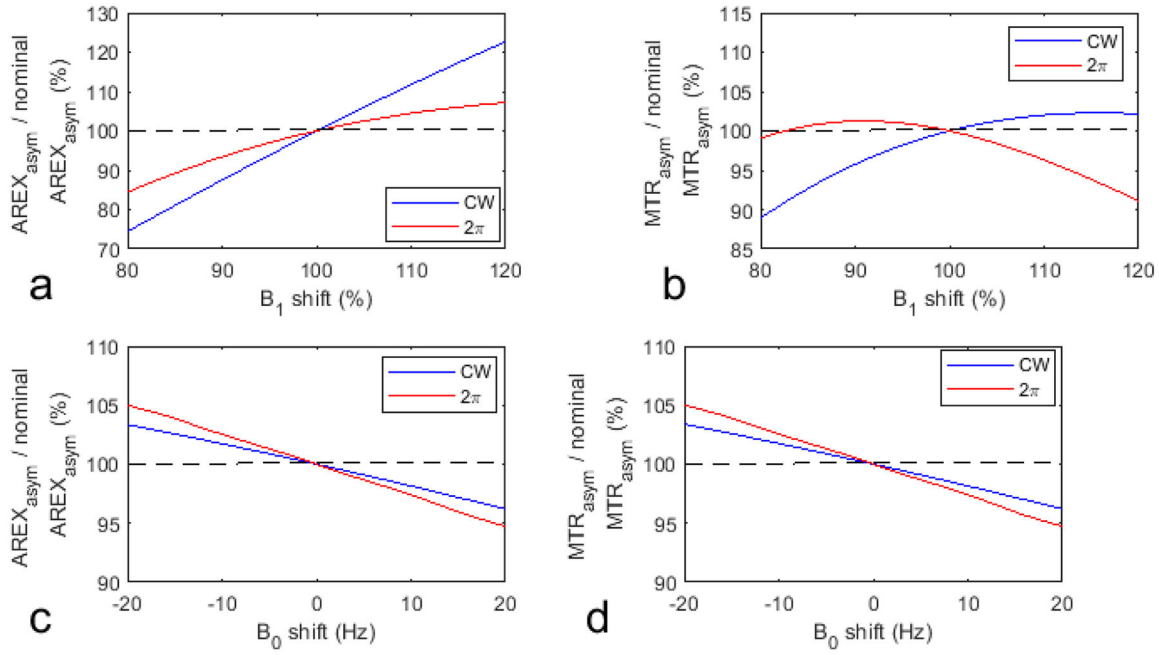

Fig. 10.

Simulated $AREX_{asym}$/nominal $AREX_{asym}$ and MTR_{asym}/nominal MTR_{asym} vs. B_1 shift (a, b) and B_0 shift (c, d). The nominal values were obtained with no B_1 and B_0 shifts.